JOURNAL OF MATERIALS SCIENCE 32 (1997) 5833–5847

Microstructure and the fracture behaviour of a Ti–24Al–11Nb intermetallic

W. O. SOBOYEJO, P. B. ASWATH*, L. XU
Department of Materials Science and Engineering, The Ohio State University, 2041 College Road, Columbus, OH 43210, USA
*and *Materials Science Program, Department of Mechanical Engineering, University of Texas at Arlington, Arlington, TX 76019, USA*

The results of a study of the effects of heat treatment on the microstructure and fracture behaviour of an α_2-based Ti–24Al–11Nb intermetallic are reported in this paper. The effects of cooling rate, annealing temperature and annealing duration on the microstructure are discussed in detail. Room- and elevated-temperature fracture mechanisms are elucidated. Toughening is shown to mainly occur by crack-tip blunting, and to a lesser extent via crack bridging and crack deflection mechanisms. A new micromechanics model is presented for the estimation of the shielding due to crack-tip blunting.

1. Introduction

There have been intensive efforts to characterize the microstructure and fracture properties of α_2-based alloys (such as Ti–24Al–11Nb) in recent years [1–16]. The microstructural studies have indicated the potential for the formation of the ordered α_2 phase based on the Ti_3Al (DO_{19} crystal structure) [6, 7], the ordered β_0 structure based on the Ti_3Al Nb (B2 crystal structure) [6, 7], an orthorhombic phase with the space group Cmcm [16], and a β type phase with a $B8_2$ structure [17]. The microstructural evolution that occurs in Ti–24Al–11Nb during thermal exposure can therefore be very complex due to the large number of phases that can be formed during thermal exposure, and the influence of microstructure on the mechanical properties is not fully understood. There is, therefore, a need for further studies designed to improve our basic understanding of the relationships between microstructure and mechanical properties in α_2-based titanium aluminides.

The results of a systematic investigation of the effects of annealing on the microstructure and fracture behaviour of $\alpha_2 + \beta$ forged Ti–24Al–11Nb are presented in this paper. The paper is divided into seven sections. The processing/heat treatment schedules and the experimental procedures are summarized in Section 2 prior to a discussion on the effects of heat treatment on microstructure in Section 3. Tensile and compressive strength are then analysed in Section 4 using simple rule-of-mixture approaches for the estimation of tensile strength. This is followed by Section 5 in which the intrinsic and extrinsic factors that control room- and elevated-temperature fracture toughness are elucidated within a micromechanics framework. Elevated-temperature crack-tip deformation and fracture mechanisms also discussed in Section 5, prior to an analysis of toughening mechanisms in Section 6. Salient conclusions arising from this work are summarized in Section 7. The paper highlights the importance of micromechanics concepts in the rationalization of strength and fracture toughness.

2. Experimental procedures

2.1 Material and microstructures

The material used in this study was supplied by the Alcoa Research Laboratory, Pittsburgh, PA, in the form of a billet. It was produced by drop forging of Ti–24Al–11Nb powder in the $\alpha_2 + \beta$ phase field. The resulting pancake had a diameter of 260 mm and a thickness of 12.3 mm. The forged billet was subsequently annealed at 1093 °C for 0.5 h, followed by a fan air cool. This resulted in the as-received Widmanstätten microstructure with aligned packets of approximately 3 μm wide elongated α_2 platelets (Fig. 1). The composition of the as-received (AR) material is summarized in Table 1. The as-received alloy had a 0.2% offset yield strength of 464 MPa, an ultimate tensile strength of 593 MPa, a total strain to failure of 3.9% and a fracture toughness of 23.4 MPa $m^{1/2}$ at room-temperature.

The effects of heat treatment on microstructure were investigated using cubic ($6.35 \times 6.35 \times 6.35$ mm) metallographic samples that were encapsulated in evacuated (approx. 10^{-4} Pa) quartz capsules prior to annealing. The heat treatment schedules were designed to investigate the following:

(1) the effects of annealing in the $\alpha_2 + \beta$ phase field;
(2) the effects of cooling rate after annealing in the β phase field; and
(3) the effects of annealing in the $\alpha_2 + \beta$ phase field after prior exposure in the β field.

The metallographic samples were ground with different grades of emery paper and polished to a mirror

TABLE I Actual chemical composition of as-received Ti–24Al–11Nb (wt %)

Ti	Al	Nb	O	C	H	N
Balance	13.4	22.1	0.075	0.017	0.0042	0.0078

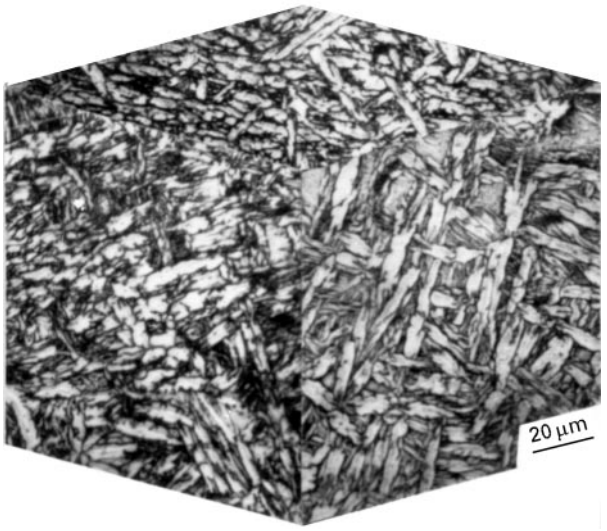

Figure 1 Microstructure of as-received Ti–24Al–11Nb.

surface finish on a 1 μm diamond wheel. The polished surfaces were then etched in Kroll's solution for approximately 10 s, prior to microstructural examination via optical, scanning and transmission electron microscopy. Further details on the microscopic techniques are provided in references [1, 2]. Quantitative estimates of the lath sizes and the prior β grain sizes were obtained using linear intercept techniques [18], and phase analyses of microstructural constituents was conducted using X-ray diffraction techniques.

2.2 Mechanical properties

The effects of heat treatment on compressive and tensile properties were investigated at room- and elevated-temperatures. The compression and tension tests were carried out at a strain rate of $5 \times 10^{-4}\,s^{-1}$. The compression tests were performed on $6.35 \times 6.35 \times 6.35$ mm cubic specimens at 25, 540, 650 and 760 °C. Tension tests were also conducted at room-temperature on smooth cylindrical specimens with a guage diameter of 3 mm. After testing, longitudinal cross-sections parallel to the axial loading direction in the deformed compression and tensile specimens were examined by optical microscopy. Microstructural features associated with deformation-induced cracking were thus identified.

Fracture toughness tests were performed at room- and an elevated-temperature (800 °C) on single edge notched (SEN) specimens. The tests were conducted under three-point bend loading after pre-cracking under far-field compression [19, 20] at a stress range, $\Delta\sigma = \sigma_{max} - \sigma_{min}$, of approximately 250 MPa, and a stress ratio, $R = \sigma_{min}/\sigma_{max}$, of 10. After pre-cracking, the fracture toughness specimens were loaded monotonically to failure at a ramp rate that corresponded to a stress intensity factor increase rate of $0.92\,MPa\,m^{1/2}\,s^{-1}$ at the crack tips. Resistance curve experiments were also performed on selected SEN specimens at room- and elevated-temperature. The resistance curve experiments were conducted under load control at 25 and 800 °C. The initial stress intensity factors were increased in 5% increments during the resistance curve experiments. Failure modes were examined in all the tensile and fracture specimens via scanning electron microscopy (SEM).

Crack-tip deformation mechanisms were examined in the resistance curve specimens using crack-tip transmission electron microscopy (TEM) techniques. The TEM specimen preparation was rather difficult, and it involved the preparation of TEM foils (diameter approximately 3 mm) by dimpling and ion milling. The crack tips were positioned at distances that corresponded to less than one cyclic plastic zone size from the centres of the TEM foils, which were examined under a TEM operated under a beam voltage of 200 kV. Further details on the TEM specimen preparation techniques are given in references [2, 20].

3. Microstructure

3.1 Effects of annealing in the $\alpha_2 + \beta$ phase field

The effects of annealing in the $\alpha_2 + \beta$ phase field in Ti–24Al–Nb are similar to those reported previously for conventional $\alpha_2 + \beta$ titanium alloys [21]. However, some unique microstructural features were also observed as discussed in this section. Annealing of Ti–24Al–11Nb in the $\alpha_2 + \beta$ phase field at 815 and 982 °C did not result in significant coarsening of the α_2 laths, and the average lath widths were approximately 3 μm before and after annealing at these temperatures (Fig. 2a and b). The alignment of the α_2 laths within the Widmanstätten colonies was maintained after annealing in the $\alpha_2 + \beta$ phase field. X-ray diffraction revealed that a small amount of orthorhombic phase [16] was formed after annealing in the $\alpha_2 + \beta$ phase field at temperatures between 815–1093 °C

More complex or prolonged thermal exposures in the $\alpha_2 + \beta$ phase field resulted in changes in microstructure (Fig. 3a–d). Prolonged annealing at 800 °C for 100 h resulted in coarsening of the α_2 laths (Fig. 3a). The Widmanstätten structure of the as received material, was, therefore stable at this temperature. Annealing at 1050 °C, followed by water quenching, led to the formation of a structure consisting of primary and Widmanstätten α_2 grains (Fig. 3b). Also, annealing at 1100 °C, followed by furnace cooling, resulted in a refined Widmanstätten microstructure (Fig. 3c), while heat treatment at 1100 °C/0.67 h/WQ + 1000 °C/0.5 h/AC + 800 °C/4h/AC, resulted in a structure consisting of primary α_2 and secondary $\alpha_2 + \beta$ (Fig. 3d). Note AC stands for air cool, WQ for water quench, FC for furnace cool.

3.2 Effects of cooling rate

Cooling rate had a strong effect on microstructure after annealing in the β phase field (Fig. 4a–c). With

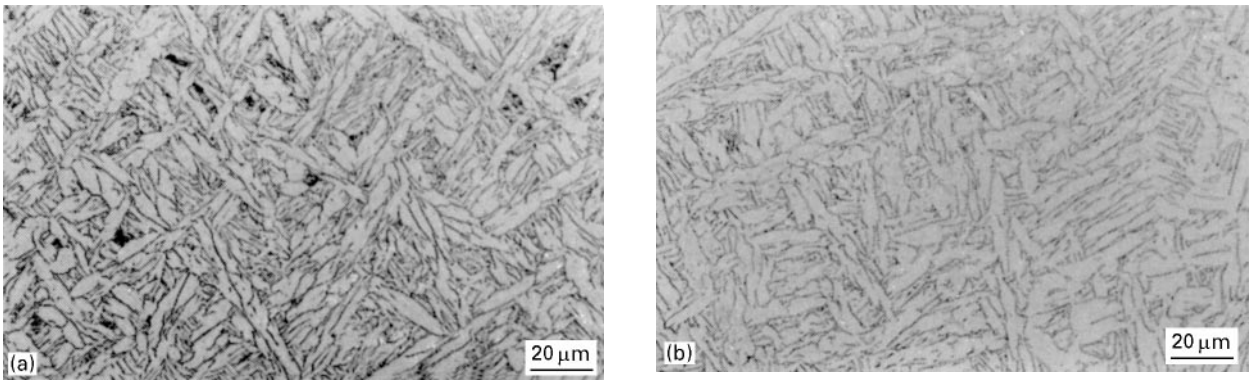

Figure 2 Effects of annealing in the $\alpha_2 + \beta$ phase field on microstructure (a) 815 °C/5.5 h/AC and (b) 982 °C/4 h/AC. AC = air cool.

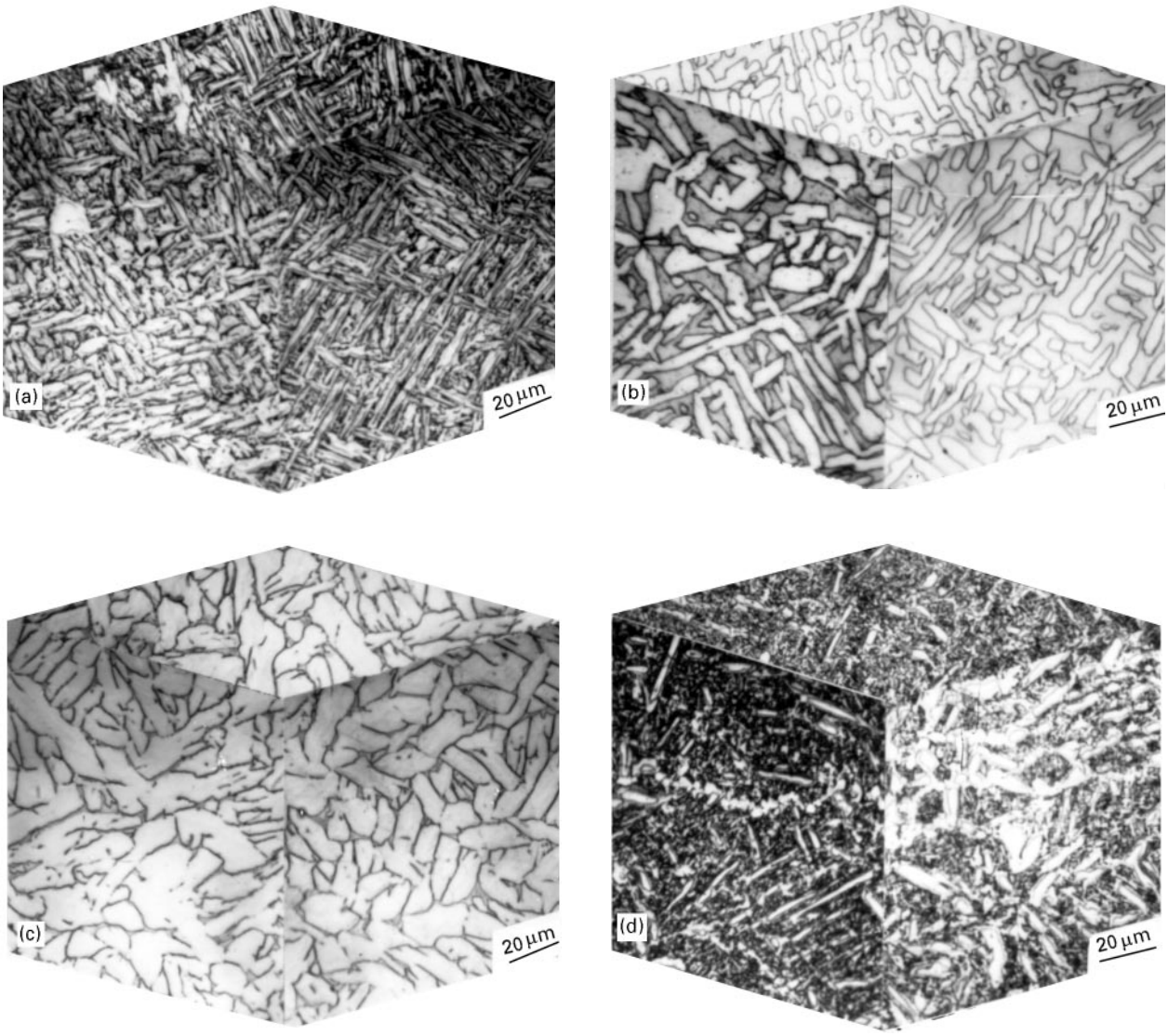

Figure 3 Effects of prolonged annealing in the $\alpha_2 + \beta$ phase field on microstructure (a) 800 °C/100 h/AC, (b) 1050 °C/20 h/WQ, (c) 1100 °C/2 h/FC, and (d) 1100 °C/0.67 h/WQ + 1000 °C/0.5 h/AC + 800 °C/4 h/AC. AC = air cool, FC = furnace cool.

the exception of fan air cooling, fast cooling from the β phase field, followed by air cooling (AC) or water quenching in quartz capsules (WQ), resulted in the formation of subgrains within large (700–1000 μm) prior β grains (Fig. 4a and b). The sub-grains are more clearly visible in the microstructure of the water quenched sample (Fig. 4a), and are presumed to form as a result of strain accommodation due to possible dislocation interactions that can occur during fast cooling from the β phase field.

Very fine acicular α_2 laths were observed at the boundaries of the prior β grain boundaries of the specimens that were subjected to fast cooling from the β phase field (Fig. 4a and b). The observed laths appear to have a well defined orientation relationship with the prior β grain boundaries, and are arranged in

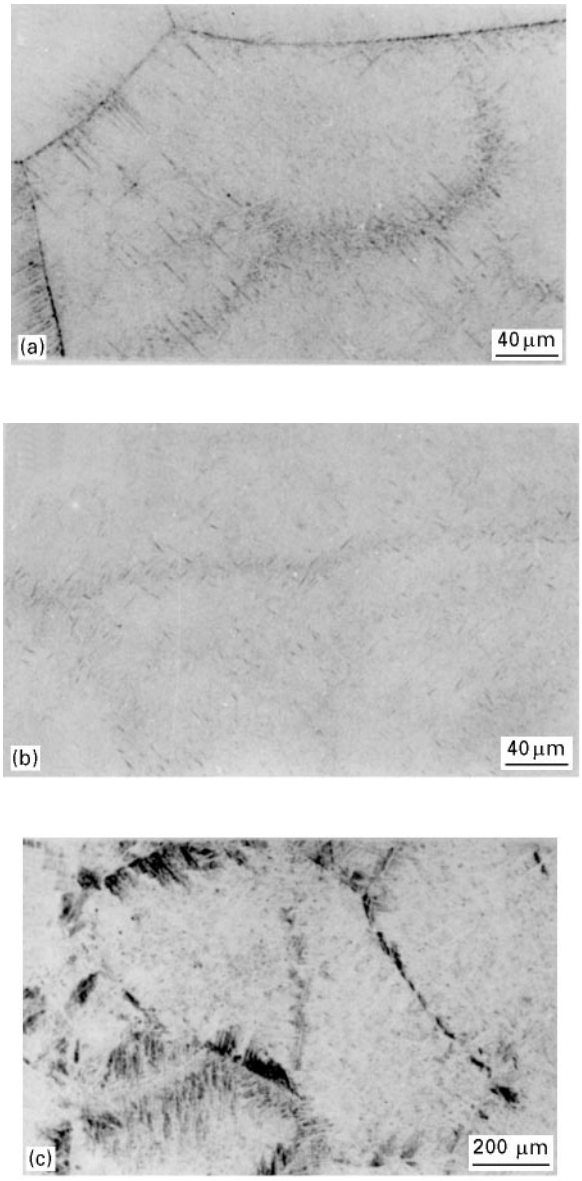

Figure 4 Effects of cooling rate from the β phase field on microstructure (a) 1200 °C/0.5 h/WQ, (b) 1200 °C/0.5 h/AC, and (c) 1200 °C/0.5 h/FC

approximately parallel strips in the vicinity of the prior β grain boundaries. This is in contrast to the randomly oriented fine α_2 laths that are observed at the subgrain boundaries (Fig. 4a and b). The α_2 lath widths also increased with decreasing cooling rate from the β phase field (Fig. 4a–c), and furnace cooling from the β phase field resulted in the formation of an inhomogeneous basket weave microstructure (Fig. 4c).

3.3 Effects of annealing in the $\alpha_2+\beta$ phase field after β heat treatment

Water quenching and fan air cooling from the β phase field, followed by ageing in the $\alpha_2+\beta$ phase field, was found to promote the formation of cracks within the allotriomorphs that were formed along the prior β grain boundaries (Fig. 5a and b). However, the α_2 lath widths within the prior beta grains did not significantly coarsen during such exposure, and the resulting lath widths were comparable to those observed in the as-received material (Figs 1 and 5a and b). Prolonged annealing in the $\alpha_2+\beta$ field at 650 °C led to the decomposition of the microstructures produced after fan air cooling from the β phase field (Fig. 5c). Note that the lighter regions in Fig. 5c are α_2 rich/β depleted zones within the prior beta grain boundaries. The microstructures produced by fast cooling from the β field and ageing in the $\alpha_2+\beta$ field are therefore unstable. In contrast, the Widmanstätten (Fig. 5d and e) and basketweave (Fig. 5f) structures produced respectively by air and furnace cooling from the β field, and annealing in the $\alpha_2+\beta$ field, remain relatively stable during thermal exposure in the $\alpha_2+\beta$ field at 650 °C for 24 h.

4. Tensile and compressive properties

4.1 Compression

The 0.2% offset yield strengths obtained at room- and elevated-temperature are summarized in Tables II and III. Attractive elevated-temperature strengths were retained at temperatures up to 760 °C. The room-temperature compression strength of the as-received material was also reduced by 40–80 MPa upon annealing, and a difference of approximately 150 MPa was observed between the room- and elevated-temperature compression strengths in the different microstructural conditions that were examined. With the exception of the anomalously high compression strength obtained at 760 °C for material annealed at 1200 °C/0.5 h/AC +815 °C/8 h/AC, the compression strengths were similar in all the microstructural conditions that were tested at temperatures between 540–760 °C. It is also important to note that there was very little ($\leqslant 0.015$ wt %) interstitial oxygen pick-up during testing at elevated temperature in air. Hence, the observed trends in the compression strength data are attributed mainly to the effects of microstructural changes.

Longitudinal cross-sections of the deformed compressive specimens revealed considerable evidence of cracking in most of the plastically deformed cubic samples (Fig. 6a–c). However, cracking was not observed in all the deformed samples (Fig. 6d and e), and the extent of cracking appeared to increase with increasing volume fraction of the β depleted zones (Fig. 6a–c). It is also clear from Fig. 6a–c that stable crack growth is retarded in the β depleted zones (lighter regions in Fig. 6a and b) and the regions containing thick α_2 allotriomorphs at the prior β grain boundaries of material annealed at 1200 °C/0.5 h/AC +760 °C/8h/AC (Fig. 6c). Such retardation may strengthen/toughen the material. Compressive deformation in Ti–24Al–11Nb therefore appears to promote discontinuous cracking prior to specimen rupture. The ultimate compressive strengths will therefore largely depend on the propagation and coalescence of the multiple cracks across the specimen widths.

4.2 Tension

The room-temperature tensile properties are summarized in Table III. The attractive total strain to

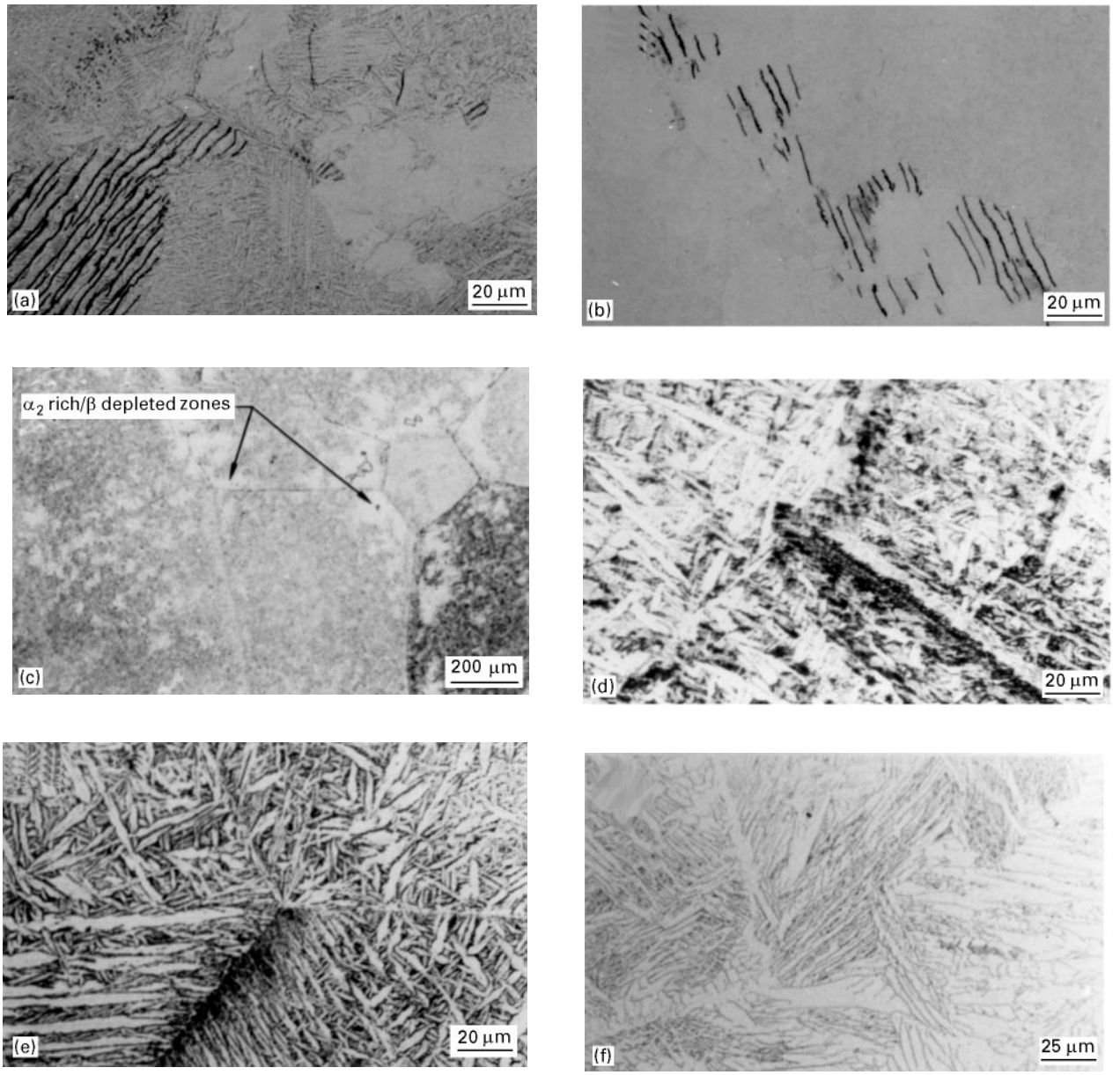

Figure 5 Effects of annealing in the β and $\alpha_2 + \beta$ phase fields on microstructure (a) 1200 °C/0.5 h/WQ + 760 °C/8 h/AC, (b) 1200 °C/0.5 h/WQ + 815 °C/8 h/AC, (c) 1200 °C/0.5 h/FAC + 650 °C/24 h/AC, (d) 1200 °C/0.5 h/AC + 760 °C/8 h/AC, (e) 1200 °C/0.5 h/AC + 815 °C/8 h/AC, and (f) 1200 °C/0.5 h/FC + 815 °C/8 h/AC.

TABLE II Effects of heat treatment on elevated-temperature compressive strengths

Heat treatment	0.2% offset compressive yield strength (MPa)		
	540 °C	650 °C	760 °C
1200 °C/0.5 h/AC + 760 °C/8 h/AC	448	453	483
1200 °C/0.5 h/AC + 815 °C/8 h/AC	486	454	640
1200 °C/0.5 h/FC + 760 °C/8 h/AC	454	430	371
815 °C/5.5 h/AC	437	438	369
982 °C/4 h/AC	384	408	338

AC = air cool, FC = furnace cool

failure (3.9%) of the as-received material was not retained after most of the heat treatments. However, a total strain to failure of 2.1% (1.4% plastic strain) was obtained after annealing at 1200 °C/0.5 h/FC + 760 °C/8 h/AC. This heat treatment, unlike all the others shown in Table III, resulted in improved tensile strengths ($\sigma_{ys} = 521$ MPa and UTS = 665 MPa). There was no clear correlation between (optical) microstructure and tensile strength (Table III), which suggests that the loss of strength and ductility was due to substructural changes. The loss of room-temperature ductility may also have been partly induced by the formation of the orthorhombic phase [16] that was detected by X-ray diffraction after annealing at temperatures between 815–1093 °C. However, further work is needed to verify this speculation.

Estimates of the strength, σ, of Ti–24Al–11Nb can be obtained by idealizing the materials as two-phase composites, consisting of α_2 and β phases. The strengths of the composites are thus given by simple rule-of-mixtures, which yields:

$$\sigma = f_\alpha \sigma_\alpha + f_\beta \sigma_\beta \quad (1)$$

TABLE III Effects of heat treatment on microstructure and room-temperature mechanical properties

Heat treatment/condition	Proportion of β phase (%)	Prior β grain size (μm)	α_2 platelet width (μm)	Fracture toughness K_{IC} (MPa m)$^{1/2}$	Tensile properties			0.2% offset compressive yield stress (MPa)	Predicted yield stress (MPa)
					Total strain to failure (%)	0.2% offset yield stress (MPa)	Ultimate tensile stress (MPa)		
As-received (1093 °C/0.5 h/FAC)	26	–	3.3	23.4	3.9	464	593	658	580
1200 °C/0.5 h/AC + 760 °C/8 h/AC	16	965	3.2	12.1	–(a)	–(a)	582	620	565
1200 °C/0.5 h/AC + 815 °C/8 h/AC	16	981	3.8	14.1	–(a)	–(a)	502	609	565
1200 °C/0.5 h/FC + 760 °C/8 h/AC	22	521	3.0	19.8	2.1	521	665	659	574
815 °C/5.5 h/AC	18	–	2.6	17.9	–(a)	–(a)	340·	577	568
982 °C/4 h/AC	21	–	3.3	18.4	–(a)	–(a)	356	682	573

(a) Fractured before yield.
NOTES:
FAC = fan air cool
AC = air cool
FC = furnace cool.

where subscripts α and β denote α and β phases, and f is the volume fraction. The constituent properties can be obtained from reference [22], which gives $\sigma_{y\alpha} =$ 540 MPa and $\sigma_{y\beta} = 695$ MPa at room temperature. Note that the single phase alloys in reference [22] fracture before yield. Nevertheless, the above data was used to obtain estimates of the "yield" strengths of Ti–24Al–11Nb in selected microstructural conditions. The predictions obtained by substitution of the single-phase strength data into Equation 1 are summarized in Table III. The predicted yield strengths were generally within $\pm 12\%$ of the measured values in the as-received material. Similar agreement was also obtained between the theoretical predictions and the measured strengths in the material that was air cooled from 1200 °C, prior to annealing in the $\alpha_2 + \beta$ phase field. However, significant differences were observed between the predicted and measured strengths of the material that was furnace-cooled from 1200 °C, and the materials that were annealed solely in the $\alpha_2 + \beta$ phase field (Table III).

The longitudinal cross-sections of the tensile specimens revealed evidence of extensive microcracking within the deformed gauge sections. This is shown in Fig. 7a–e. Cracking was observed to occur in the beta matrix and across the α_2 grains, and there was evidence of multiple crack initiation from the α_2 case that was observed on the sides of the tensile specimens (Fig. 7a). Final fracture occurred by the coalescence of multiple microcracks (Fig. 7b, d and e). It is interesting to note here that a lower incidence of cracking was observed in materials that exhibited some plastic strain to failure (Fig. 7e) than that in the material that fractured before yield (Fig. 7a–d). However, in general, the fracture behaviour of Ti–24Al–11Nb was found to largely depend on the propagation and coalescence of microcracks that were initiated mainly in the beta depleted zones.

Typical fracture surface morphologies observed in the tensile specimens are presented in Fig. 8(a–f). Failure generally occurred by transgranular cleavage after annealing in the $\alpha_2 + \beta$ phase field (Fig. 8a–c). Such annealing resulted in highly faceted transgranular cleavage fracture modes with river lines that are characteristic of cleavage fracture. Annealing at 1200 °C/0.5 h/FC + 760 °C/8 h/AC resulted in a transgranular cleavage fracture mode and fluting across the boundaries of the α_2 grains (Fig. 8d). Such fluting may be due to the effects of crack-tip blunting by the matrix beta phase. However, further work is needed to verify this speculation. Also, β heat treatment followed by air cooling and annealing in the $\alpha_2 + \beta$ phase field resulted in a rough transgranular cleavage fracture mode (Fig. 8e and f).

5. Fracture toughness

The room-temperature fracture toughness data are summarized in Tables III and IV. The highest room-temperature fracture toughness value of 23.4 MPa m$^{1/2}$ was obtained in the as-received condition. This high fracture toughness value was also associated with the highest β volume fraction (Table III). The

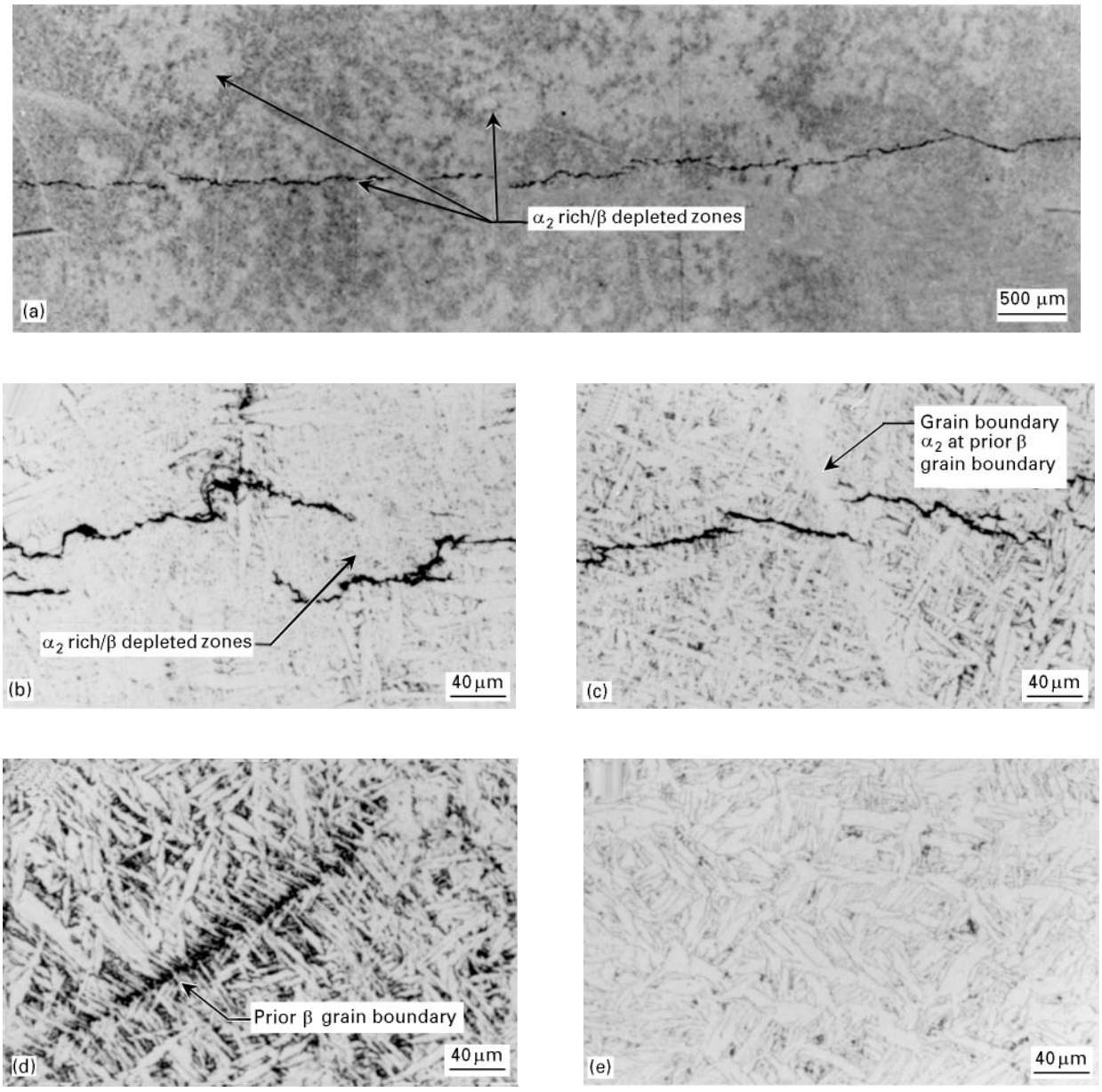

Figure 6 Longitudinal cross-sections of compression specimens deformed at 25 °C (a–c) 1200 °C/0.5 h/AC + 760 °C/8 h/AC, (d) 1200 °C/0.5 h/AC + 815 °C/8 h/AC, and (e) 815 °C/5.5 h/AC.

fracture toughness of the as-received material increased to 28 MPa $m^{1/2}$ at 700 °C. The relatively high fracture toughness of 19.8 MPa $m^{1/2}$ obtained by annealing at 1200 °C/0.5 h/FC + 760 °C/8 h/AC was associated with an inhomogeneous basket weave microstructure (Fig. 5f) and a very rough transgranular cleavage fracture surface morphology (Fig. 9a and b). Less tortuous crack paths were observed in the other microstructures that were examined, and failure generally occurred by a relatively flat transgranular cleavage fracture mode (Fig. 9c and d). The basket weave structure (Fig. 4f) formed after annealing at 1200 °C/0.5 h/FC + 760 °C/8 h/FC had a fracture toughness of 19.8 MPa $m^{1/2}$. The basket weave microstructure and fracture toughness were largely retained, even after subsequent thermal exposure in the $\alpha_2 + \beta$ field at 650 °C for 100 h, which resulted in a fracture toughness of 18.8 MPa $m^{1/2}$.

Annealing at 800 °C for 100 h, followed by an air cool (Fig. 3a), resulted in a significant loss of room-temperature fracture toughness from approximately 24 to 13 MPa $m^{1/2}$. The same heat treatment resulted in a fracture toughness of 36 MPa $m^{1/2}$ at 700 °C. However, the mixed primary α_2/Widmanstätten structure formed after annealing at 1050 °C and water quenching (Fig. 3b) had a room-temperature fracture toughness of 20 MPa $m^{1/2}$. This structure resulted in a fracture toughness of 30 MPa $m^{1/2}$ at 700 °C. The Widmanstätten structure formed after annealing at 1100 °C and furnace cooling (Fig. 3c) had a fracture toughness of 17 MPa $m^{1/2}$ at room-temperature, and a fracture toughness of 20 MPa $m^{1/2}$ at 700 °C. Similarly, the mixed primary $\alpha_2/\alpha_2 + \beta$ structure formed after annealing at 1100 °C/0.67 h/FC + 1000 °C/0.5 h/FC + 800 °C/4 h/AC (Fig. 3d) had a room-temperature fracture toughness of 15 MPa $m^{1/2}$, and a fracture toughness of 32 MPa $m^{1/2}$ at 700 °C (Table IV).

Fracture toughness therefore significantly increased with increasing temperature in the selected

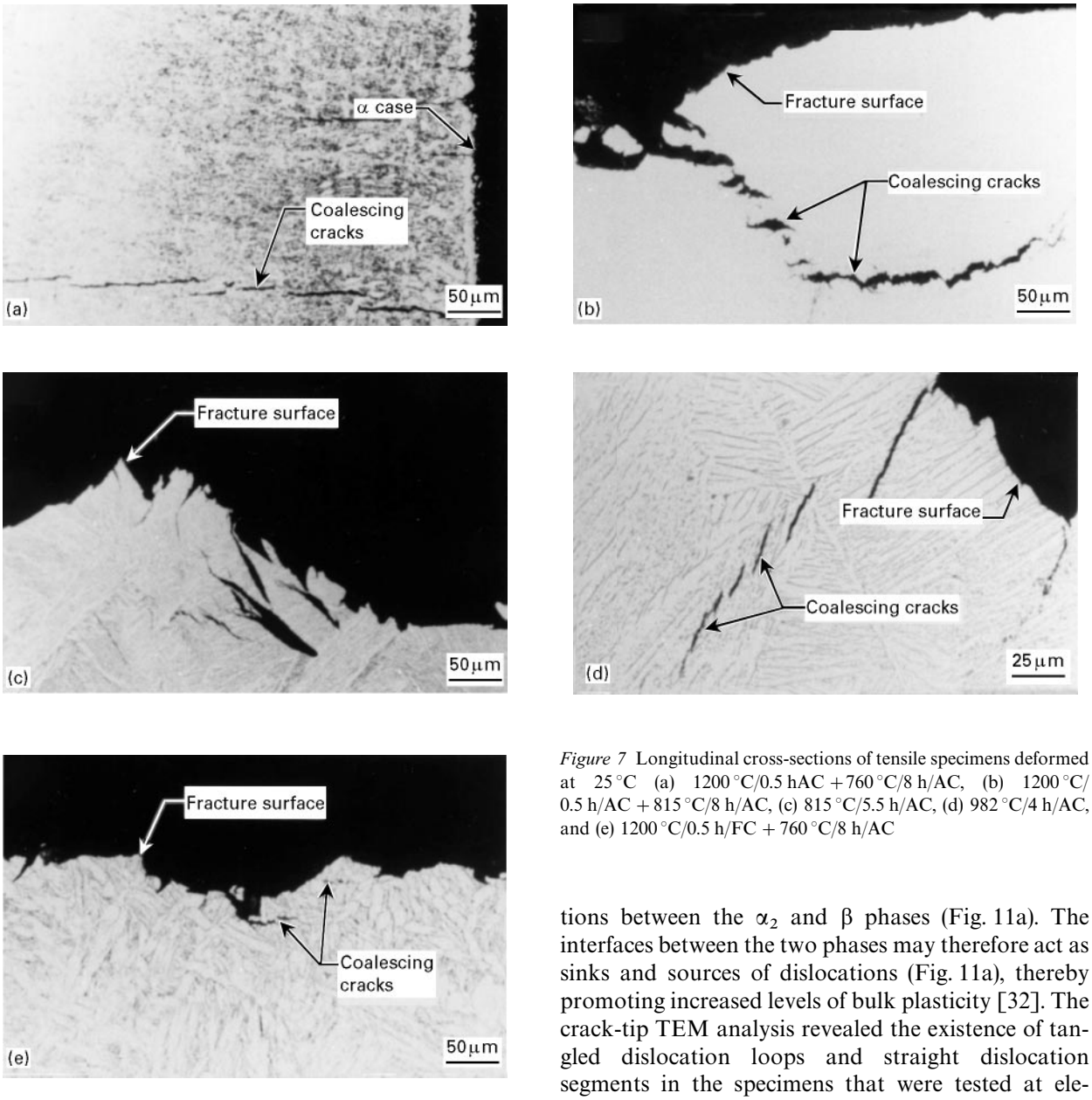

Figure 7 Longitudinal cross-sections of tensile specimens deformed at 25 °C (a) 1200 °C/0.5 hAC + 760 °C/8 h/AC, (b) 1200 °C/0.5 h/AC + 815 °C/8 h/AC, (c) 815 °C/5.5 h/AC, (d) 982 °C/4 h/AC, and (e) 1200 °C/0.5 h/FC + 760 °C/8 h/AC

microstructural conditions that were examined. This increase is partly attributed to the higher levels of plasticity (increase in slip activity) at elevated-temperature [31]. However, fracture at elevated-temperature was associated with cleavage (Fig. 10a) and intergranular (Fig. 10b) failure modes, in spite of the increased plasticity. Intergranular failure occurred across the prior beta grains in the fracture toughness specimens that were tested at elevated-temperature. Planar slip markings were also observed on the cleaved α_2 facets, and evidence of plastic stretching was observed in the beta phase (Fig. 10a). Profuse microcracking was generally associated with stable crack growth at elevated-temperature (Fig. 10c), and the extension of the main crack occurred via crack coalescence (Fig. 10c), as observed in a recent study by Davidson *et al.* [15]. The microcrack distributions may promote shielding or anti-shielding, depending on their spatial configurations.

The crack-tip TEM analysis of the resistance curve specimens revealed the existence of interfacial dislocations between the α_2 and β phases (Fig. 11a). The interfaces between the two phases may therefore act as sinks and sources of dislocations (Fig. 11a), thereby promoting increased levels of bulk plasticity [32]. The crack-tip TEM analysis revealed the existence of tangled dislocation loops and straight dislocation segments in the specimens that were tested at elevated-temperature (Fig. 11b). Such dense dislocation networks were not observed in previous crack-tip deformation studies at room-temperature [2], or in the undeformed microstructures that were examined after processing and/or heat treatment (Fig. 11c). The higher elevated-temperature fracture toughness levels may therefore be partly attributed to the higher levels of plasticity. These contribute to the observed differences in the room- and elevated-temperature *R*-curve behaviour shown in Fig. 12a and b. However, improved understanding of the trends in the fracture toughness and *R*-curve data requires some consideration of the toughening mechanisms, which are discussed in detail in the next section.

6. Toughening mechanisms

6.1 Introduction

The role of intrinsic and extrinsic crack-tip shielding mechanisms will be examined in this section using micromechanics models. The models will be used for the assessment of crack-tip blunting, crack bridging, crack deflection and micro-crack shielding/anti-

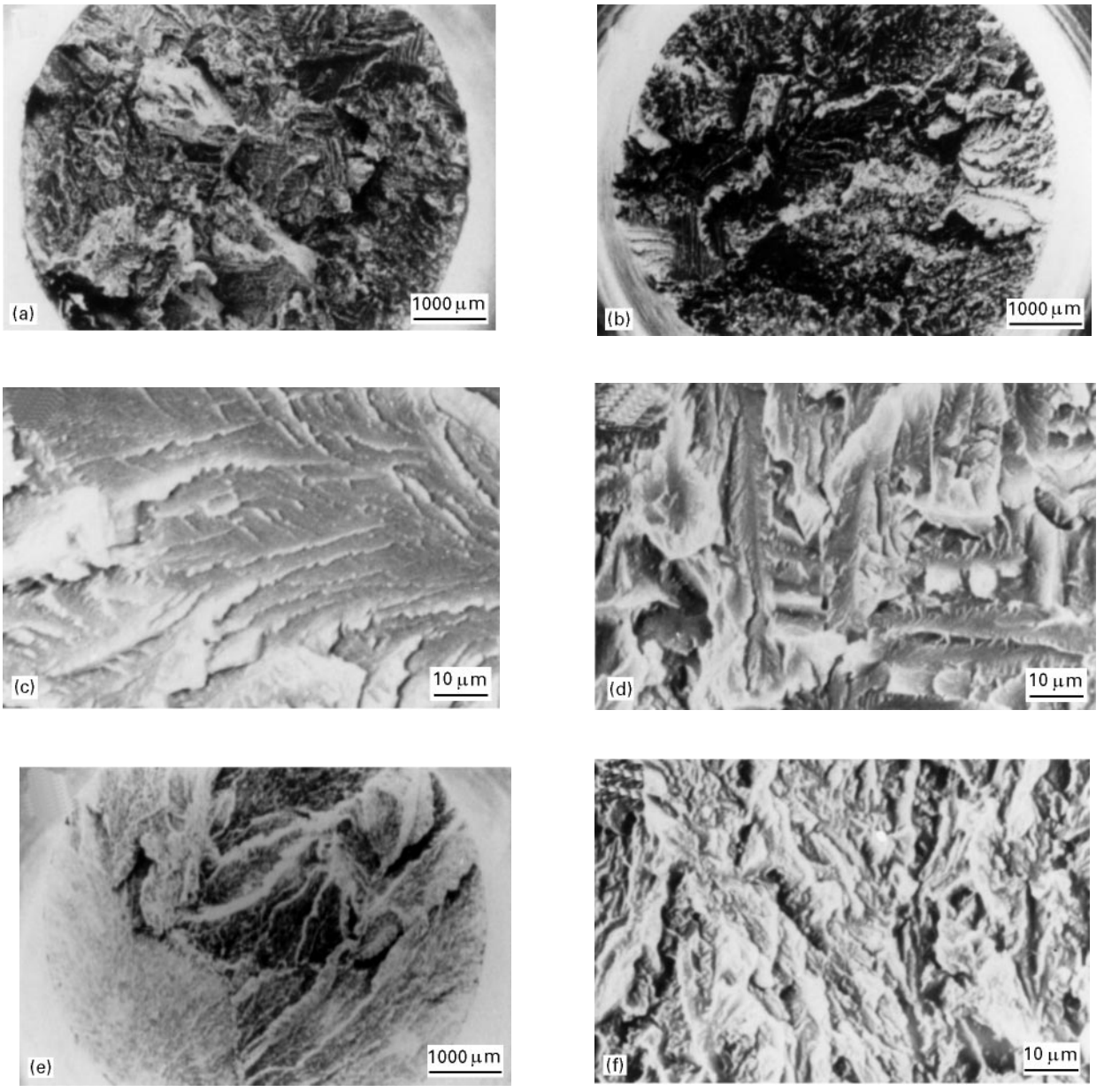

Figure 8 Fracture surface morphologies of smooth cylindrical specimens deformed to failure in tension at room-temperature (a) 982 °C/4 h/AC, (b, c) 815 °C/5.5 h/AC, (d) 1200 °C/0.5 h/FC + 760 °C/8 h/AC, and (e, f) 1200 °C/0.5 h/AC + 760 °C/8 h/AC.

TABLE IV Comparison of room- and elevated-temperature fracture toughness data

Heat treatment/condition	Fracture toughness (MPa $m^{1/2}$)	
	25 °C	700 °C
As-received	23	28
800 °C/100 h/AC	13	36
1050 °C/20 h/AC	20	30
1100 °C/2 h/FC	17	20
1100 °C/0.67 h/WQ + 1000 °C/0.5 h/AC + 800 °C/4 h/AC	15	32

shielding [23–30]. Two methods will be presented for the estimation of the shielding due to crack-tip blunting by the β phase. These include: a new micromechanics model, and a model developed by Chan [23]. Due to complexities associated with the possible effects of time-dependent plasticity effects at elevated-temperature, the discussion will focus on the analysis of toughening at room-temperature. Toughening predictions will be presented for selected microstructures with continuous and discontinuous β phases.

6.2 Crack-tip blunting

6.2.1 Chan's model

Chan's model [23] was originally developed to assess the effects of crack-tip blunting on the fracture toughness of Ti–24Al–11Nb. He argued that although fractographic analysis generally revealed cleavage-like features in Ti–24Al–11Nb, the fracture could be considered as a ductile process since the fracture appearance was the result of cracking along planar slip bands via processes involving localized plastic deformation and high normal stresses (in the slip band). Thus, by assuming that fracture is controlled by a critical strain criterion, he postulated that the

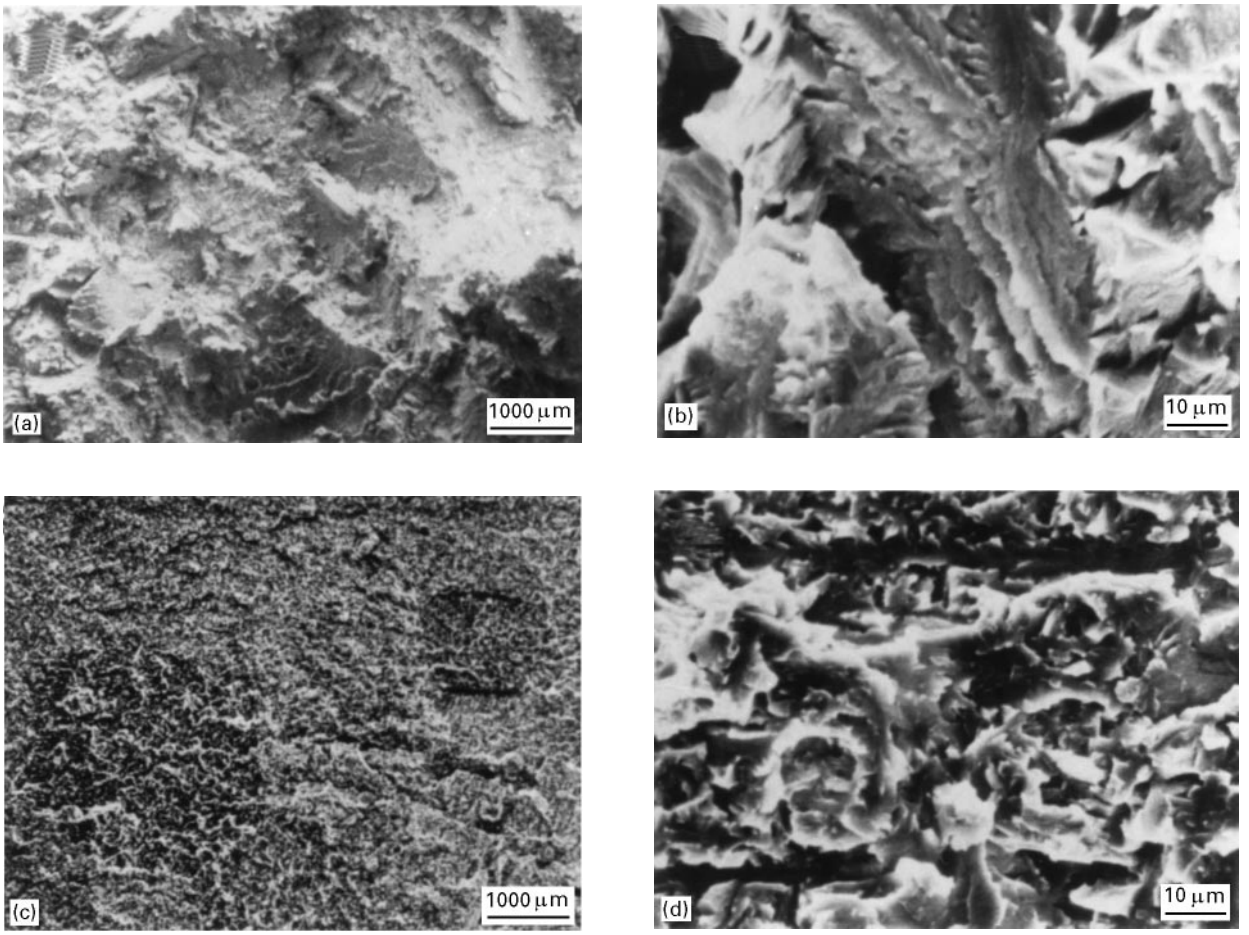

Figure 9 Fracture surface morphologies of room-temperature fracture toughness specimens annealed in the β and/or $\alpha_2 + \beta$ phase fields (a, b) 1200 °C/0.5 h/FC + 760 °C/8 h/AC and (c, d) 1200 °C/0.5 h/AC + 760 °C/8 h/AC.

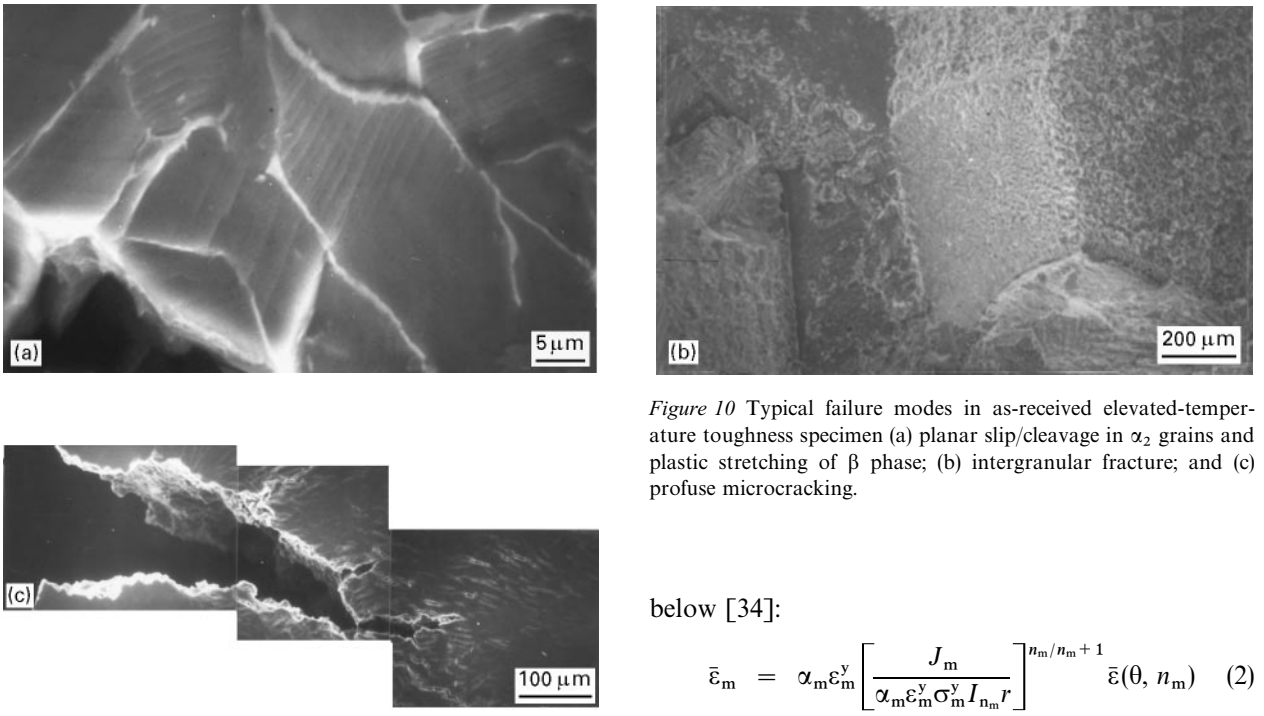

Figure 10 Typical failure modes in as-received elevated-temperature toughness specimen (a) planar slip/cleavage in α_2 grains and plastic stretching of β phase; (b) intergranular fracture; and (c) profuse microcracking.

near-tip effective strain distribution in the matrix/composite in a ductile phase reinforced brittle matrix composite could both be described by Hutchinson–Rice–Rosengren (HRR) field expressions given below [34]:

$$\bar{\varepsilon}_m = \alpha_m \varepsilon_m^y \left[\frac{J_m}{\alpha_m \varepsilon_m^y \sigma_m^y I_{n_m} r} \right]^{n_m/n_m+1} \bar{\varepsilon}(\theta, n_m) \quad (2)$$

and

$$\bar{\varepsilon}_c = \alpha_c \varepsilon_c^y \left[\frac{J_c}{\alpha_c \varepsilon_c^y \sigma_c^y I_{n_c} r} \right]^{n_c/n_c+1} \bar{\varepsilon}(\theta, n_c) \quad (3)$$

where subscripts *m* and *c* represent matrix and composite respectively, superscript *y* represents yield

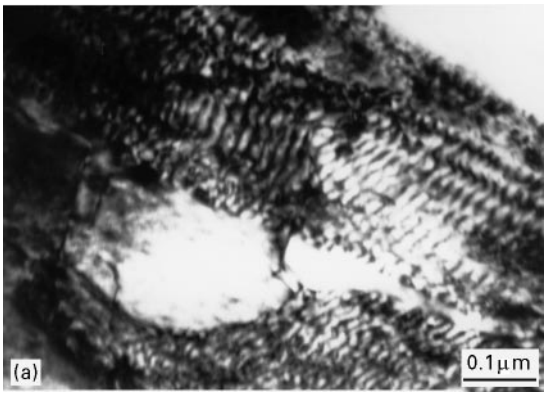

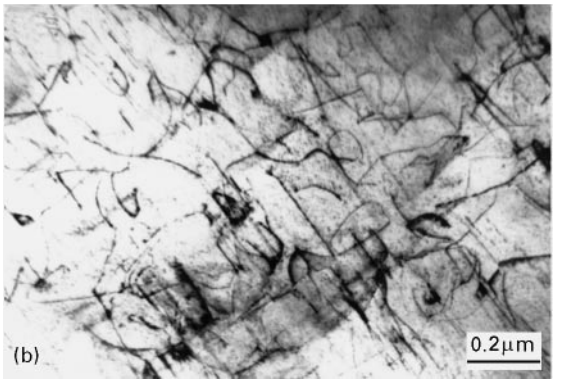

Figure 11 TEM Images of typical crack-tip and undeformed regions in as-received material. (a) Interfacial dislocations in crack-tip region, (b) straight and bowed dislocations in crack-tip region, and (c) low dislocation density in undeformed material.

stress, J_m and J_c are path independent parameters (J integrals) that vary with the applied load, crack length, and the geometry of the specimen, I_{n_m} and I_{n_c} are numerical constants the values of which depend on the stress relation of the material, $\bar{\varepsilon}(\theta, n_m)$ and $\bar{\varepsilon}(\theta, n_c)$ are also numerical constants related to the angle away from the crack plane at a particular n value, α_m, α_c, n_m and n_c are constants in the Ramberg–Osgood stress strain relation which is given by:

$$\frac{\varepsilon}{\varepsilon_y} = \frac{\sigma}{\sigma_y} + \alpha\left[\frac{\sigma}{\sigma_y}\right]^n \quad (4)$$

where σ_y and ε_y are yield stress and strain respectively, n is the strain hardening exponent, and α is a dimensionless material constant. The second term on the right side of Equation 4 describes the plastic or non-

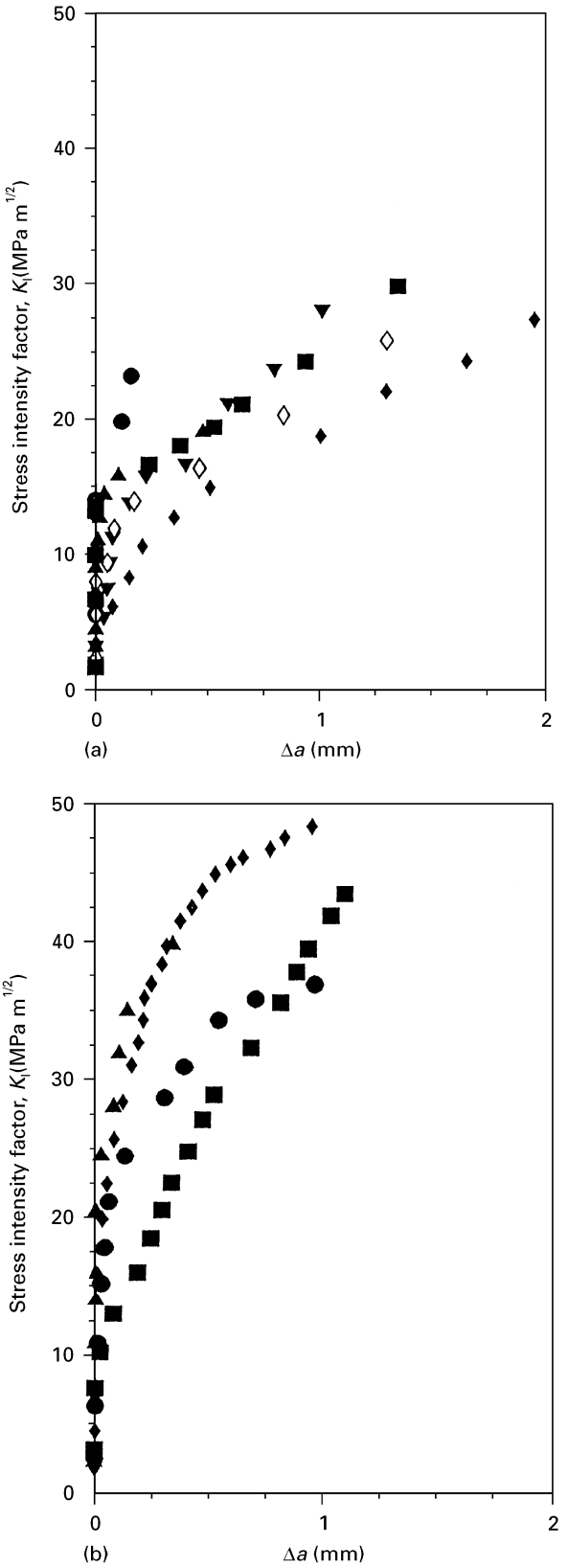

Figure 12 Resistance curves after heat treatment obtained at (a) 25 °C. Key: (■) as received (AR: 1093 °C/0.5 h/FAC), (◆) AR + 800 °C/100 h/AC, (◇) AR + 1150 °C/20 h 50 min/WQ, (●) AR + 1050 °C/20 h/BWQ, (▼) AR + 1100 °C/2 h/FC and (▲) AR + 1100 °C/40 min/BWQ + 1000 °C/0.5 h/AC + 800 °C/4 h/AC and (b) 700 °C: Key: (■) as received (AR: 1093 °C/0.5 h/FAC), (◆) AR + 800 °C/100 h/AC, (▲) AR + 1150 °C/2 h 50 min/WQ and (●) AR + 1050 °C/20 h/BWQ. Note: FAC, far air cooled; AC, air cool; FC, furnace cool; BWQ, bath water quench.

linear behaviour. By assuming that the stress strain behaviour is the same in both the matrix and

composite, i.e., $\alpha_m = \alpha_c = \alpha$ and $n_m = n_c = n$, the following expression is obtained by dividing Equation 3 by Equation 2:

$$\frac{\bar{\varepsilon}_c}{\bar{\varepsilon}_m} = \frac{\varepsilon_c^y}{\varepsilon_m^y}\left[\frac{J_c}{J_m}\right]^{n/n+1}\left[\frac{\varepsilon_m^y \sigma_m^y}{\varepsilon_c^y \sigma_c^y}\right]^{n/n+1} \quad (5)$$

By invoking $\varepsilon_c^y = \sigma_c^y/E_c$, $\varepsilon_m^y = \sigma_m^y/E_m$, $J_c = (1-\upsilon_c^2)K_c^2/E_c$, and $(1-\upsilon_m^2)/E_m$ and rearranging both sides of the resulting equation, Equation 5 reduces to:

$$\frac{K_c}{K_m} = \left[\frac{\sigma_c^y}{\sigma_m^y}\right]^{n-1/2n}\left[\frac{\bar{\varepsilon}_c}{\bar{\varepsilon}_m}\right]^{n+1/2n}\left[\frac{E_c}{E_m}\right]^{n+1/2n} \quad (6)$$

The toughening ratio, which is defined as the ratio of the applied stress intensity factor to the stress intensity factor in the matrix, is thus given by:

$$\lambda_b = \frac{K_\infty}{K_m} = \frac{K_c}{K_m} = \left[\frac{\sigma_c^y}{\sigma_m^y}\right]^{n-1/2n}\left[\frac{\bar{\varepsilon}_c}{\bar{\varepsilon}_m}\right]^{n+1/2n}\left[\frac{E_c}{E_m}\right]^{n+1/2n} \quad (7)$$

where λ_b is the toughening ratio due to crack tip blunting, K_∞ is the applied stress intensity factor. Other terms have been defined previously. The above equation for the toughening ratio for crack-tip blunting, λ_b, may also be expressed as:

$$\lambda_b = \frac{K_\infty}{K_m} = [1 + V_\beta(\Sigma - 1)]^{(N-1)/2N} \times [1 + V_\beta(\Gamma - 1)^{(N+1)/2N}\left[\frac{E_c}{E_m}\right]^{(N+1)/2N} \quad (8)$$

with

$$\Sigma = \frac{\sigma_y^\beta}{\sigma_y^\alpha} \quad (9)$$

and

$$\Gamma = \frac{\varepsilon_f^\beta}{\varepsilon_f^\alpha} \quad (10)$$

where K_m is the fracture toughness of the α_2 matrix [31], σ_y is the yield stress, ε_f is the fracture strain, N is the inverse of the strain hardening exponent, n, E_m is the matrix modulus and subscripts α and β denote α and β phases, respectively. Comparisons of the tensile properties of a single phase α_2 [31] and β [33, 34] titanium alloys suggests that appropriate values for Σ and Λ are 1.2 and 5, respectively. By substituting these values of Σ and Λ, and $n = 18$ into Equation 8, it is easy to compute the toughening ratio, λ_b, and the fracture toughness due to blunting, i.e.,

$$K_b = \lambda_b K_m \quad (11)$$

The predicted fracture toughness values due to blunting by the β phase, K_b, are compared with the measured fracture toughness values in Table V. As in previous studies [1, 23], there is good agreement between the predicted toughness due to crack-tip blunting and the measured fracture toughness values in materials with continuous β phase. However, the predicted fracture toughness values are greater than the measured values in the materials with discontinuous β phase. The good agreement between the predicted K_b and the measured K_{Ic} values in material with continuous β phase suggests that toughening in Ti–24Al–11Nb is largely due to the intrinsic effects of crack-tip blunting mechanisms. However, the predicted fracture toughness values, K_b, are generally less than the measured fracture toughness values, K_{Ic}.

The differences between the measured and predicted fracture toughness values are attributed to potential crack-tip shielding by crack bridging [23], deflection [24, 25], and microcracking [26–29] mechanisms. The differences between the measured and predicted data are also partly due to experimental scatter and inherent limitations of the above crack-tip blunting model. A new model was therefore developed in an attempt to improve the overall accuracy of the fracture toughness predictions.

6.2.2. The new model

Chan's original work [23] treated the crack-tip blunting in a Ti–24Al–11Nb alloy in which the fracture strain for the hard α_2 phase was approximately 5%. However, the α_2 phase is generally known to undergo much less plastic deformation than the $\alpha_2 + \beta$ Ti–24Al–11Nb material. Hence, the assumption that the HRR field can be used to describe the near tip strain field both in the composite and the matrix may not be fully valid. In fact, due to the brittle nature of

TABLE V Comparison of toughening predictions from the Chan model [23] and the new model

Heat treatment/condition	β phase		Intrinsic toughening Chan model		New model		Measured fracture toughness K_{IC} (MPa m$^{1/2}$)
	β volume fraction	Continuous β phase yes/no	λ_b	ΔK_b (MPa m$^{1/2}$)	λ_b	ΔK_b (MPa m$^{1/2}$)	
As-received (1093 °C/0.5 h/FAC)	26	Yes	1.56	7.0	1.64	7.6	23.4
1200 °C/0.5 h/AC + 760 °C/8 h/AC	16	No	1.32	4.0	1.45	5.6	12.1
1200 °C/0.5 h/AC + 815 °C/8 h/AC	16	No	1.32	4.0	1.45	5.6	14.1
1200 °C/0.5 h/FC + 760 °C/8 h/AC	22	Yes	1.41	5.1	1.57	7.1	19.8
815 °C/5.5 h/AC	18	Yes	1.38	4.8	1.50	6.3	17.9
982 °C/4 h/AC	21	Yes	1.40	5.0	1.55	6.9	18.4

NOTES: K_m = Matrix fracture toughness = 12.5 MPa m$^{1/2}$ [22]. FAC = fan air cooled, AC = air cool, FC = furnace cool

the matrix, an elastic crack-tip stress field is more likely to describe the stress distribution in the matrix [34]. In the plastic region, the strain field in the composite can be described by the HRR expression given in Equation 2. In the elastic region, the strain in the composite is:

$$\bar{\varepsilon}_c = \frac{K_c}{E_c}\frac{1}{(2\pi r)^{1/2}}\bar{\varepsilon}(\theta) \quad (12)$$

where K_c and E_c are the stress intensity factor and Young's modulus of the composite, $\bar{\varepsilon}_c(\theta)$ is a function of orientation, and r is the distance from the crack-tip. Equations 3 and 12 can be reformulated as:

$$\left(\frac{\bar{\varepsilon}_c}{\alpha_c\varepsilon_c^y}\right)^{(n+1)/n} = \frac{J_c}{\alpha_c\varepsilon_c^y\sigma_c^y}\frac{1}{I_n r}[\bar{\varepsilon}_c(\theta, n_c)]^{(n+1)/n} \quad (13)$$

and

$$(\bar{\varepsilon}_c)^2 = \left(\frac{K_c}{E_c}\right)^2\frac{1}{2\pi r}[\bar{\varepsilon}_c(\theta)]^2 \quad (14)$$

At the junction between the elastic and plastic regions, $\bar{\varepsilon}_c = \varepsilon_c^y$. Equations 13 and 14 can be combined with :

$$J_c = \frac{(1-\upsilon_c^2)K_c^2}{E_c} \quad (15)$$

leading to:

$$\frac{[\bar{\varepsilon}_c(\theta, n_c)]^{(n+1)/n}}{[\bar{\varepsilon}_c(\theta)]^2}\frac{1}{I_n}\frac{(1-\upsilon_c^2)}{\alpha_c(1/\alpha_c)^{(n+1)/n}} = \frac{1}{2\pi} \quad (16)$$

For the matrix, the near-tip strain field can be expressed as:

$$(\bar{\varepsilon}_m)^2 = \left(\frac{K_m}{E_m}\right)^2\frac{1}{2\pi r}[\bar{\varepsilon}_m(\theta)]^2 \quad (17)$$

Since $\bar{\varepsilon}_m(\theta) = \bar{\varepsilon}_c(\theta)$, combining Equations 13–17 gives:

$$\frac{K_c}{K_m} = \frac{E_c}{E_m}\frac{(\bar{\varepsilon}_c)^{(n+1)/2n}}{\bar{\varepsilon}_m}(\varepsilon_c^y)^{(n-1)/2n} \quad (18)$$

Hence, the modified blunting toughening ratio is given by:

$$\lambda_b = \frac{K_\infty}{K_m} = \frac{K_c}{K_m} = \frac{E_c}{E_m}\frac{(\bar{\varepsilon}_c^f)^{(n+1)/2n}}{(\bar{\varepsilon}_m^f)}(\varepsilon_c^y)^{(n-1)/2n} \quad (19)$$

Toughening ratio estimates obtained from the modified crack-tip blunting model are compared with those obtained from Chan's model [23] in Table V. The toughening ratio predictions obtained from the new model are slightly higher than those predicted by the Chan model [23]. This result is intuitively obvious since the HRR field expressions may overestimate the crack-tip fields in an elastic material. Conversely, the assumption of purely elastic behaviour in the brittle matrix material is likely to underestimate the actual crack-tip fields in nearly elastic materials. The most representative toughening ratios are therefore likely to be in between those predicted by the Chan model [23] and the new model. Nevertheless, the new model will be used in subsequent discussion, since it is likely to provide a better representation of the crack-tip stress field in the brittle α_2 matrix than the Chan model [23].

6.3 Crack bridging

Extrinsic toughening due to crack bridging by the β phase has been shown to occur in Ti–24Al–11Nb [23]. This can be modelled using the following expression derived by Budiansky *et al.* [30] for the toughening ratio, λ_{br}, due to plastic stretching of β ligaments with a fracture stress, σ_f:

$$\lambda_{br} = \frac{K_\infty}{K_m} = 1 + 2\left(\frac{2}{\pi}\right)^{1/2}\left(\frac{V_f\sigma_f L^{1/2}}{K_m}\right) \quad (20)$$

where L is the length of the β bridge which is approximately equal to the average length of the elongated α_2 grains, and V_f is the β volume fraction. Predictions of the "extrinsic" toughening ratio, λ_{br}, and the fracture toughness, ΔK_{br}, are summarized in Table VI. These show quite clearly that the toughening contributions due to crack bridging by β ligaments are much less than those due to crack-tip blunting. However, the toughening due to crack bridging, ΔK_{br}, can be used to explain the fracture toughness values of the materials with discontinuous β phase, e.g., the materials that were annealed at 1200 °C/0.5 h/AC + 760 °C/8 h/AC or 1200 °C/0.5 h/AC + 815 °C/8 h/AC (Table VI).

The combined intrinsic and extrinsic toughening due to the presence of the β phase can be estimated using the principle of superposition. However, the predicted overall fracture toughness values are generally below the measured fracture toughness values. This indicates the potential significance of the crack deflection [24, 25] and microcrack shielding [26–29] mechanisms which will be discussed in the next two sections.

6.4 Crack deflection

Crack-tip shielding due to deflection can be estimated from the mode I and mode II stress intensity factors, K_I and K_{II}, induced at the crack-tip as a result of deflection via tilting through an angle ϕ[24, 25]. This results in K_I and K_{II} values that are given by:

$$K_I = \cos^2(\phi/2)K_\infty \quad (21)$$

and

$$K_{II} = \sin(\phi/2)\cos^2(\phi/2)K_\infty \quad (22)$$

Equations 21 and 22 can be combined to obtain the following expression for λ_d, the toughening ratio due to crack deflection:

$$\lambda_d = \frac{K_\infty}{K_m} = \frac{1}{\cos^2(\phi/2)} \quad (23)$$

Predicted toughening increments, ΔK_d, based on λ_d are presented in Table VI. These show that crack deflection has only a small effect of crack-tip shielding levels. This was largely due to the fact that the deflection angles were generally too small to induce significant levels of crack-tip shielding. Nevertheless, it is important to note that although crack deflection did not result in significant crack-tip shielding, it does appear to account for most of the differences between

TABLE VI Comparison of toughening predictions and measured fracture toughness values

Heat treatment condition	β volume fraction (%)	Continuous β phase (yes/no)	Blunting by β phase		Bridging by β phase		Crack deflection		Total toughening		Measured toughness
			λ_{b1}	ΔK_{b1} (MPa m$^{1/2}$)	λ_{br}	ΔK_{br} (MPa m$^{1/2}$)	λ_d	ΔK_d (MPa m$^{1/2}$)	ΔK_t (MPa m$^{1/2}$)	K_t	K_{IC} (MPa m$^{1/2}$)
As-received (1093 °C/0.5 h/FAC)	26	Yes	1.64	7.6	1.12	1.5	1.01	0.1	9.2	21.7	23.4
1200 °C/0.5 h/AC + 760 °C/8 h/AC	16	No	1.45	5.6	1.07	0.9	1.03	0.4	6.9	19.4	12.1
1200 °C/0.5 h/AC + 815 °C/8 h/AC	16	No	1.45	5.6	1.07	0.9	1.03	0.4	6.9	19.4	14.1
1200 °C/0.5 h/FC + 760 °C/8 h/AC	22	Yes	1.57	7.1	1.09	1.1	1.06	0.8	9.0	21.5	19.8
815 °C/5.5 h/AC	18	Yes	1.50	6.3	1.08	1.0	1.01	0.1	7.4	19.9	17.9
982 °C/4 h/AC	21	Yes	1.55	6.9	1.10	1.3	1.01	0.1	8.3	20.8	18.4

the measured fracture toughness values and the toughening due to combined effects of crack bridging and crack-tip blunting by the β phase, as shown in Table VI.

6.5 Micro-crack shielding/anti-shielding

The final extrinsic toughening mechanisms that can be of interest involves crack-tip shielding by microcracks in the wake of the crack tip. The shielding due to microcracks has been modelled by a number of investigators for single [26] and multiple [27–29] cracks.

Since only a limited number of microcracks with relatively wide separations were observed at room-temperature, the shielding effects of the microcracks at room-temperature can be treated individually using the analysis due to Rose [26] in which the change in the stress intensity of the dominant crack, ΔK_i, is given by:

$$\Delta K_i = \Delta\sigma_i^P (2\pi R_1)^{1/2} F_i(S, R_1, \theta_1, \alpha_1, \Delta\sigma_i^P) \quad (24)$$

where $2S$ is the length of the microcrack located at radial distance, R_1, and an angle of Θ_1, from the crack tip, α_1, is the orientation of the microcrack with respect to the stress axis, and the values of $F_i(S, R_1, \theta_1, \alpha_1, \Delta\sigma_i^P)$ are given by polynomial expressions due to Rose [26]. The toughening ratio due to microcracking λ_m is given by:

$$\lambda_m = \frac{K_\infty}{K} = \frac{K_\infty}{[(K_\infty + \Delta K_I^P)^2 + (\Delta K_{II}^P)^2]^{1/2}} \quad (25)$$

where λ_m in Equation 25, is less than unity, then microcracks ahead of the crack tip result in embrittlement or anti-shielding. Conversely, values of λ_m greater than unity result in toughening by the microcracks. The extent of anti-shielding or extrinsic toughening largely depends on the angle between the microcracks and the dominant crack [26]. The angle, Θ_1, was observed to be close to zero, and only a small amount of anti-shielding was predicted in the microstructures that were examined. The shielding contributions from microcracking are therefore negligible at room-temperature. However, micro-crack shielding may be important at elevated-temperature, although its effects are difficult to quantify due to the complex configurations of microcracks that are generally observed at elevated-temperature (Fig. 10c). Further work is clearly needed to develop the tools for the assessment of toughening components at elevated-temperature.

7. Conclusions

(1) Annealing of the as-received material solely in the $\alpha_2 + \beta$ phase field at 815 and 982 °C does not result in significant coarsening of the α_2 laths in the Widmanstätten microstructure that is produced after the $\alpha_2 + \beta$ processing and fast cooling. However, such

annealing promotes significant degradation of strength and ductility, presumably as a result of substructural or submicroscopic changes.

(2) Fast cooling from the β phase field promotes the formation of subgrains within the prior β grains. These subgrains are presumed to form as a result of strain accommodation during quenching from the β phase field, and are annealed out during further thermal exposure at 760 and 815 °C. Randomly oriented α_2 laths are nucleated at the subgrain boundaries, and parallel strips of α_2 laths are nucleated at the prior β grain boundaries after fast cooling from the β phase field. Annealing in the $\alpha_2 + \beta$ phase field after quenching from the β phase field promotes the formation of cracks at prior β grain boundaries.

(3) Prolonged annealing in the $\alpha_2 + \beta$ phase field, after fast cooling from the β phase field, promotes the formation of grain boundary α_2 allotriomorphs and significant microstructural decomposition. This is accompanied by the formation of the orthorhombic phase after annealing at temperatures between 815–1093 °C. However, a relatively stable basketweave microstructure, with a good balance of properties, is obtained by furnace cooling from the β phase field and annealing in the $\alpha_2 + \beta$ phase field at 760 °C.

(4) The compression strengths are similar in the materials with the Widmanstätten and basket weave microstructures. Compression strengths for these microstructures decrease from approximately 620 MPa at 25 °C, to approximately 450 MPa at elevated temperatures between 540–760 °C. Damage in compression involves the initiation, linkage, and growth of microcracks. Similar damage modes are observed in the room-temperature tensile specimens.

(5) Toughening in Ti–24Al–11Nb with continuous β microstructures is largely due to crack-tip blunting by the β phase. However, the shielding contributions from crack bridging and crack deflection must also be considered for a complete rationalization of the measured fracture toughness data. Toughening in material with discontinuous β phase can be explained by considering the combined effects of crack bridging and crack deflection. Improved elevated-temperature fracture toughness is attributed to higher levels of crack-tip plasticity, and the possible effects of microcracking shielding at elevated-temperature.

Acknowledgements

The authors are grateful to Messrs. F. Ye, E. Petersen, J. J. Evans, B. A. Abbott, J. E. O'Neal and J. D. Keyes for assistance with the preparation of this paper. Appreciation is also extended to Prof. S. M. L. Sastry and Prof. S. Suresh for useful discussions. This research at OSU (WOS and LX) was supported by McDonnell Douglas Aerospace, and a grant from The Divison of Materials Research of The National Science Foundation (Grant No. DMR 9458018), with Dr. Bruce MacDonald as Program Monitor. PBA was also supported by a grant from The National Science Foundation (Grant No. MSS-9108891), with Dr. William Spitzig as Program Monitor.

References

1. W. O. SOBOYEJO, *Metall. Trans.* **23A** (1992) 1737.
2. P. B. ASWATH, Ph.D. thesis, Brown University, Providence, RI, (1990).
3. H. T. KESTNER-WEYKAMP, C. H. WARD, T. F. BRODERICK and M. J. KAUFMAN, *Scripta Metall.* **23** (1989) 1697.
4. W. O. SOBOYEJO, in Proceedings 7th World Conference on Titanium, San Diego, August 1993, edited by F. H. Froes and I. L. Kaplan (The Metallurgical Society, Warrendale, PA, 1993) vol. 1, p. 359.
5. D. B. KNORR and N. S. STOLOFF, *Mater. Sci. Engng* **A123** (1990) 81.
6. A. K. GOGIA, D. BANERJEE and T. K. NANDY, *Metall. Trans.* **21A** (1990) 609.
7. A. K. GOGIA, T. K. NANDY, D. BANERJEE and Y. MAHAJAN, in Proceedings 6th World Conference on Titanium, edited by P. Lacombe, R. Tricot and G. Beringer, Suppl. to *J. Phys.* (1988) 1097.
8. D. BANERJEE, A. K. GOGIA and T. K. NANDY, *Metall. Trans.* **21A** (1990) 627.
9. C. WARD, *Int. Met. Revs* **38** (1993) 79.
10. P. B. ASWATH and S. SURESH, *Mater. Sci. Engng* **A114** (1989) L1.
11. P. B. ASWATH, W. O. SOBOYEJO, and S. SURESH, in "Fatigue '90", edited by K. Tanaka and H. Kitagawa (Materials and Components Engineering Publications Ltd., Warley, UK, 1990) Vol. III, p. 1941.
12. P. B. ASWATH and S. SURESH, *Metall. Trans.* **22** (1991) 817.
13. *idem*, in "Elevated temperature crack growth", edited by S. Mall and T. Nicholas (ASME Publications, New York, NY, 1990) p. 69.
14. C. H. WARD, A. W. THOMPSON and J. C. WILLIAMS, *Metall. Trans.* **26A** (1995) 703.
15. D. L. DAVIDSON, J. B. CAMPBELL and R. A. PAGE, *ibid.* **22A** (1991) 377.
16. D. BANERJEE, A. K. GOGIA, T. K. NANDY and V. A. JOSHI, *Acta Metall.* **36** (1988) 871.
17. R. STRYCHOR, J. C. WILLIAMS and W. A. SOFFA, *Metall. Trans.* **19A** (1988) 225.
18. R. T. DEHOFF and F. N. RHINES, Eds., "Quantitative microscopy" (McGraw Hill, New York NY, 1968).
19. S. SURESH and J. R. BROCKENBROUGH, *Acta Metall.* **36** (1988) 1455.
20. W. O. SOBOYEJO and C. MERCER, *Scripta Metall. Mater.* **30** (1994) 1515.
21. J. C. CHESNUTT, C. G. RHODES and J. C. WILLIAMS, in "Fractography-microscopic cracking processes," ASTM STP 600 (American Society For Testing and materials, Philadelphia PA, 1976) p. 99.
22. S. GITTIS and D. A. KOSS, in "High temperature ordered intermetallic alloys lll," edited by C. Koch and N. S. Stoloff (Materials Research Society, Pittsburgh, PA, 1989) p. 323.
23. K. S. CHAN, *Metall. Trans.* **23A** (1992) 183.
24. S. SURESH, *ibid.* **16A** (1985) 249.
25. B. COTTRELL and J. R. RICE, *Int. J. Fracture* **16** (1980) 155.
26. L. R. F. ROSE, *ibid.* **31** (1986) 233.
27. R. G. HOAGLAND and J. D. EMBURY, *J. Amer. Ceram. Soc.* **63** (1980) 404.
28. A. G. EVANS and K. T. FABER, in "Fracture in ceramics materials", edited by A. G. Evans, (Noyes Publications, Park Ridge, NJ, 1984) p. 109.
29. J. W. HUTCHINSON, *Acta Metall.* **35** (1987) 1605.
30. B. BUDIANSKY, J. C. AMAZIGO and A. G. EVANS, *J. Mech. Phys. Solids* **36** (1988) 167.
31. H. A. LIPSITT, D. SHECHTMAN and R. E. SCHAFRIK, *Metall. Trans.* **11** 1369.
32. W. O. SOBOYEJO, D. S. SCHWARTZ and S. M. L. SASTRY, *ibid.* **23A** (1992) 2039.
33. F. H. FROES, D. EYLON and H. B. BOMBERGER, "Titanium technology: present status and future trends (Titanium Development Association, Boulder, CO, 1985).
34. J. W. HUTCHINSON, *J. Appl. Mech.* **50** (1983) 1042.

Received 1 May 1995
and accepted 1 December 1996